

Polar Jet Stream Fluctuations in an Energy Balance Model

Cord Perillo¹, David Klein², Rabia Djellouli³

Abstract. We investigate the effect of increased greenhouse gas concentrations on the zonally averaged location of the jet stream boundary of the polar cell in a latitude dependent, two-layer Energy Balance Model. The model includes separate terms for atmospheric and surface albedos, and takes into account reflections of shortwave radiation between the surface and atmospheric layers. We introduce the notion of a cloud factor function, which depends on temperature gradients, to simulate the cell structure of Earth's global atmospheric circulation. A simulation of increased greenhouse gas concentrations initially results in a poleward movement of the polar jet stream's mean latitude, but as the concentration increases the jet moves equatorward. When the model takes both the atmospheric and the surface temperature gradients into account, under high concentrations the location of the jet stream becomes unstable and quasi-periodic as its mean location moves equatorward.

INDEX TERMS: energy balance model, polar jet fluctuations, temperature gradient, quasi-periodicity

¹Department of Mathematics and Interdisciplinary Research Institute for the Sciences, California State University, Northridge, Northridge, CA 91330-8313. Email: cord.perillo@csun.edu.

²Department of Mathematics and Interdisciplinary Research Institute for the Sciences, California State University, Northridge, Northridge, CA 91330-8313. Email: david.klein@csun.edu. Orcid ID: <https://orcid.org/0000-0003-1964-4378>

³Department of Mathematics and Interdisciplinary Research Institute for the Sciences, California State University, Northridge, Northridge, CA 91330-8313. Email: rabia.djellouli@csun.edu.

1 Introduction

The atmosphere and the ocean stabilize Earth’s climate from uneven solar insolation by transporting heat from the equator to the poles. Energy balance models (EBMs), first introduced by Budyko [7], Sellers [41], include heat transport terms that reproduce zonally and annually averaged temperature profiles from this transport. These idealized climate models have been extensively studied (e.g. North [32, 33, 34]) and a wide range of modifications and additional forcings have been introduced in order to provide insights into causal relationships of components of Earth’s climate, for example, [11, 18, 20, 31, 24, 45, 42, 5] among many other studies.

In this paper, we use an energy balance model to investigate the dynamics of the polar jet stream of an aqua-planet in response to increasing greenhouse gas concentrations, with a focus on the role of cloud fraction and albedo. Both observations and climate model studies indicate that the general circulation pattern of the atmosphere is altered by anthropogenic warming, e.g., [4, 13, 17, 22, 27, 28, 50, 51]. Among these are two studies that employed EBMs to investigate the link between shifts of the midlatitude storm tracks to the shifts of the Hadley cell edge, Mbengue and Schneider [30] (hereafter MS18) and and Siler, Roe, Armour [40] (hereafter SRA18).

MS18 [30] defined the storm track in a one layer EBM as the latitude of maximum absolute value of the temperature gradient. In that model, the diffusion coefficient was increased within the Hadley cell, relative to the diffusion coefficient outside the cell, and the Hadley cell edge (or terminus) was interactive and also depended on the convective lapse rate γ in the tropics, which was treated as a parameter. The model predicts that storm tracks shift in tandem as the Hadley cell edge is moved poleward by decreasing γ . Their results also indicate that strengthening meridional temperature gradient at the Hadley cell terminus can reduce the distance between the Hadley cell edge and the storm tracks, resulting in storm tracks that do not parallel shifts of the Hadley cell terminus.

SRA18 [40] studied a single layer Moist Energy Balance perturbation model. Assuming a reference climate determined by reanalysis or averages of climate models, their perturbation model determines a change in temperature and in evaporation minus precipitation, $E - P$, as a function of latitude, from forcings such as increased greenhouse gas concentrations. The extratropical latitude of the minimum value of $E - P$ serves as the proxy for mid-latitude storm tracks. In the case of spatially uniform radiative forcing, SRA18 [40] found that down-gradient energy transport implies a poleward expansion of the subtropics, where $E - P > 0$, and a poleward shift in the extratropical minimum of $E - P$, consistent with a poleward shift of storm-track latitudes.

The idealized model considered in this paper is a latitude dependent, two-layer energy balance model that includes separate terms for atmospheric and sur-

face albedos, and takes into account reflections of shortwave radiation between the surface and atmospheric layers, and includes heat diffusion terms for each layer. The novel feature of our model is what we refer to as a “cloud factor function”, a function which depends on temperature gradients, and which dynamically simulates the cell structure of Earth’s global atmospheric circulation. More specifically, the cloud factor function, $\mathcal{C}_f(\theta)$, is a dimensionless quantity that represents the fraction of the zonally averaged planetary albedo at latitude θ attributable to clouds. $\mathcal{C}_f(\theta)$ is the mechanism by which our model takes into account the influence of Earth’s rotation on the atmospheric general circulation. We use it to construct the atmospheric albedo as a function of latitude at each time step in our model (see Section 2.1 below).

The thermal wind equations link the horizontal temperature gradient to the polar jet stream and suggest that the most stable regions of the jet stream are located where the magnitude of the temperature gradient is maximized, the same proxy utilized as in MS18 [30]. Similar to MS18 [30], we interpret the latitude where this occurs as the averaged southern boundary of the Northern Hemispheric polar cell, and define our cloud factor function to achieve a maximum value at that location at each time step in our numerical scheme. This allows us to track the polar cell as it moves dynamically with each time step until the system reaches equilibrium.

We must point out that the Hadley cell edge is not interactive. We hold it fixed at 30° latitude in our numerical experiments. However, this location can easily be modified, and the qualitative behavior of our model is robust with respect to this location. Despite this constraint, our model identifies a driver of polar jet stream fluctuations, which has the potential to be incorporated into more complex climate models that include Hadley cell dynamics.

The cloud factor function, $\mathcal{C}_f(\theta)$ is constructed so that its minimum and maximum values can be interpreted as the primary cell boundaries of the global circulation. $\mathcal{C}_f(\theta)$, is a cubic Hermite spline continuously differentiable at all latitudes in a hemisphere with specified values at the equator, the Hadley cell boundary, the location of the polar jet stream, and the pole. We model it in two different ways. In the first case, called “Model One”, the location of the polar jet is determined by a gradient of the atmospheric temperature. In the second case, called “Model Two”, the location of the jet is determined by a gradient of the average of the atmospheric and surface temperatures. The two versions exhibit the same general qualitative behavior, but Model Two also exhibits instabilities and quasi-periodic behavior with interesting and suggestive physical interpretations (see Subsection 3.2).

This paper is organized as follows. Section 2 is divided into subsections that describe the components of our model, including standard forcings, but which focus primarily on the couplings between the cloud factor function and the surface and atmospheric albedos. We also describe how the latitude, where the maximum magnitude of the temperature gradient occurs at each time step of our computations, alters the cloud factor function for the next time step. Section 3 describes the results of numerical experiments for changes in the polar cell boundary as radiative forcing increases, such as from increasing greenhouse gas concentrations. In Section 4, we compare the behavior of our model with other investigations of jet stream response to increasing greenhouse gas concentrations and offer concluding remarks. In addition there are three appendices. Appendix A gives an explicit formula for the cloud factor function; Appendix B provides

a concise description of the numerical scheme used in our computations; and Appendix C displays output data for Model Two.

2 Model Description

Our EBM consists of an ocean covered surface layer and an overlying atmospheric layer. Throughout, we let $x = \sin \phi$, where ϕ is latitude⁴, so that $-1 \leq x \leq 1$, but because our aqua-planet is symmetrical, we will generally display data only for the northern hemisphere, $0 \leq x \leq 1$.

Let T_s and T_a represent the zonally averaged temperatures of the surface and atmosphere respectively. Here T_a is a measure of the free tropospheric temperature, say at 500 hPa, but as in [38] we express it as an equivalent surface air temperature, assuming a constant lapse rate (depending on the value of parameters used in the model)⁵. The time evolution of the temperatures are solutions to coupled differential equations of the form,

$$C_a \frac{\partial T_a}{\partial t} = F_{atm}^\downarrow + F_{up} - F_{out} - \frac{1}{2\pi a^2} \frac{d\mathcal{H}_a}{dx} \quad (1a)$$

$$C_s \frac{\partial T_s}{\partial t} = F_{ground}^\downarrow - F_{up} - \frac{1}{2\pi a^2} \frac{d\mathcal{H}_s}{dx}, \quad (1b)$$

where a is the radius of Earth, C_a, C_s are respectively specific heats of the atmosphere and surface, F_{out} is the longwave radiative heat flux to space, and F_{up} is heat flux from the ocean to the atmosphere from all sources. The last terms in each equation represent meridional diffusive heat transport (given explicitly in Eqs (16a) and (16b) below). Although multiple processes are involved in heat transport and although they vary across regions and time scales, Stone (1978) [46] demonstrated that the magnitude of the annual mean total meridional heat transport is insensitive to the details of dynamics of the atmosphere-ocean system.

As described below, these terms will be chosen to match the corresponding terms in the two layer energy balance model of Rose and Marshall [38, 39]. By contrast, the remaining two terms, F_{atm}^\downarrow and F_{ground}^\downarrow , in Eqs. (1a) and (1b) represent incoming solar radiation flux and both depend on the atmospheric albedo, α_a , and ground albedo, α_g .

To model the dependence of F_{atm}^\downarrow and F_{ground}^\downarrow on α_a , and α_g , we follow Qu and Hall [37] and Donohoe and Battisti [10]. We assume an atmospheric layer within which the radiation undergoes three processes: reflection by a factor α_a , transmission by a factor \mathcal{T}_{sw} (the transmissivity of shortwave radiation), and absorption by a factor $A_{sw} = 1 - \alpha_a - \mathcal{T}_{sw}$.

Summing up the infinite number of transmissions and reflections between the atmosphere and the ground, the total downwelling flux to the ground F_{ground}^\downarrow , the net flux into the atmosphere F_{atm}^\downarrow , and the total upwelling flux at the top of the atmosphere (TOA), F_{TOA}^\uparrow are given by,

⁴This formula assumes that ϕ is measured in radians. Later, in the context of temperature gradients, it will be calculated as $x = \sin(\pi\theta/180)$ where θ is given in degrees.

⁵In particular we will vary the parameter A_{out} in Eq. (16a) to simulate changes in greenhouse gas concentrations

$$F_{ground}^{\downarrow} = \frac{(1 - \alpha_g)\mathcal{T}_{sw} S_0 s(x)}{(1 - \alpha_a \alpha_g) 4} \quad (2)$$

$$F_{atm}^{\downarrow} = (1 - \alpha_g - \mathcal{T}_{sw})\left(1 + \frac{\alpha_g \mathcal{T}_{sw}}{1 - \alpha_a \alpha_g}\right) \frac{S_0 s(x)}{4} \quad (3)$$

$$F_{TOA}^{\uparrow} = \left(\alpha_a + \frac{\mathcal{T}_{sw}^2 \alpha_g}{1 - \alpha_a \alpha_g}\right) \frac{S_0 s(x)}{4} \quad (4)$$

where $s(x)$ is the annual weight function for incoming solar radiation (dimensionless, unit global mean) which, following [38, 39], is given in terms of the second order Legendre polynomial $P_2(x)$ as,

$$s(x) = 1 + s_2 P_2(x), \quad (5)$$

with $s_2 = -0.48$.

From the last expression, the planetary albedo is identified as,

$$\alpha_p = \alpha_{p,atm} + \alpha_{p,ground} = \alpha_a + \mathcal{T}_e \alpha_g \quad (6)$$

where

$$\mathcal{T}_e = \frac{\mathcal{T}_{sw}^2}{1 - \alpha_a \alpha_g}, \quad (7)$$

and $\mathcal{T}_e \alpha_g$ can be considered as the contribution from the ground albedo α_g to the planetary albedo modulated by the interactions with the atmosphere.

2.1 Cloud Factor Function

In order to assign latitudinal values to the ground and atmospheric albedos, α_g and α_a , we first introduce a *cloud factor function*, $\mathcal{C}_f = \mathcal{C}_f(\theta)$, a dynamic function of latitude $\theta = \theta(x)$. The function \mathcal{C}_f represents the fraction of the zonally averaged planetary albedo at latitude θ attributable to clouds (see Eq.(9) below). It is the mechanism by which our model takes into account the influence of planetary rotation on the accumulation of clouds by the global atmospheric circulation.

Consistent with earlier studies, Liu et al. [26] found that the planetary rotation has a strong effect on the cell structure of the atmosphere and, in particular, the Hadley cell becomes narrower and weaker with a higher planetary rotation rate. Liu et al. [26] found that the magnitudes of cloud adjustments with rotation are comparable to, or exceed, the magnitude of the climatological ocean heat uptake, and concluded that in energetic terms cloud variations are arguably more important than ocean transport variations in meridional heat transport.

It is difficult to measure cloud cover in the polar regions due to a number of factors: thin and low lying clouds, low visibility between clouds and the underlying surface, and polar conditions create an unusual amount of near surface hazes and fogs [8]. Because of these problems, there is an uncertainty in cloud cover over the polar regions. Vavrus et al. [49] conclude maximum cloudiness occurs over open water in the summer time, with cloud fraction values of 81%. Palm et al. [35] agree that maximum cloudiness occurs over open water in the summer time but report model cloud fraction values of 90%. Both conclude that the average polar cloud fraction is increasing as the sea ice extent has been decreasing.

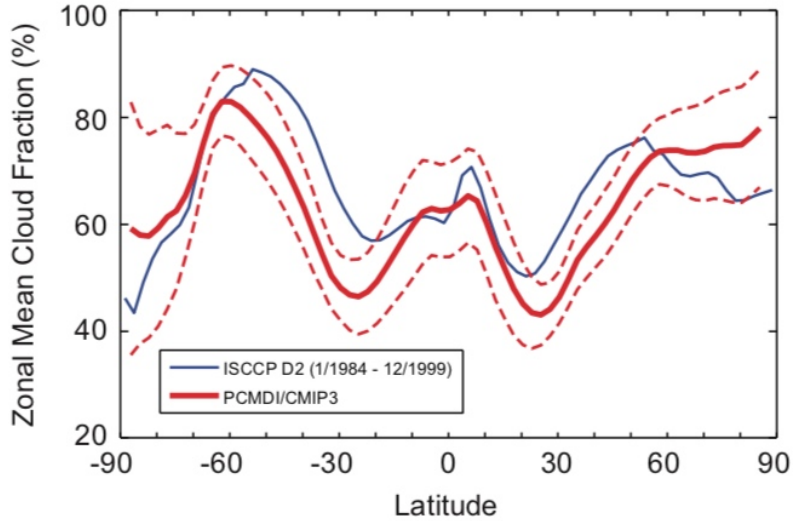


Figure 1: Zonal mean cloud fraction from CMIP3 models and compared to observations (International Satellite Cloud Climatology Project, ISCCP).⁷

Taking these findings into consideration, we construct $\mathcal{C}_f(\theta)$ through the use of cubic Hermite splines.⁸ The cloud factor function is incorporated into our climate model as described in Section 2.5. The graph of the cloud factor function is initially constrained to take extremal values at 0° , 30° , 50° , and 90° latitude, the boundaries of an initial idealized cell structure of the general circulation. Specifically, the coordinates are $(0, 0.9)$, $(30, 0.1)$, $(50, 0.9)$ and $(90, 0.9)$ so as to represent high cloudiness at the equator as well as from 50° degrees and poleward, and low cloudiness at 30° degrees, but, as we explain in Sect. 2.5, the graph will change with the time steps in the numerical runs of our models. A sample graph is shown in Figure 2.

As pointed out in [29], the Southern Hemisphere polar jet is stable at 50° latitude. So this is a plausible choice for an initial location of the polar jet prior to radiative forcings that we will impose. We note that the EBM of SAR18 [40] locates the initial northern hemisphere minimum value of $E - P$ (evaporation minus precipitation and the proxy in that EBM for storm track location) above 60° latitude (see Figures 2f and 3b in [40]).

⁷Figure from Stocker 2020 edition [44]

⁸Cubic Hermite splines are continuously differentiable at all points, including juncture points. We note that the use of linear splines instead of cubic splines results in qualitative similar final results.

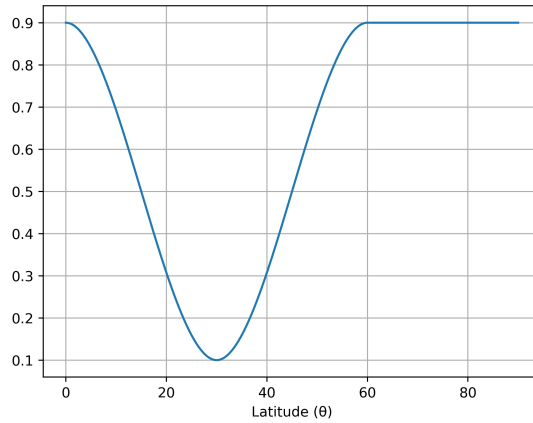


Figure 2: Cubic Hermite spline cloud factor \mathcal{C}_f plotted as a function of latitude from equator to pole with the first extratropical maximum at 60° latitude. In general, the location of the the first extratropical maximum is interactive and varies in time. See equation 19 in Appendix A.

2.2 Albedo Functions

Our modeling of the atmospheric albedo α_a and the ground albedo α_g begins with an initial approximate estimate of the planetary albedo. As a reference frame and a guide, Figure 3 shows the zonal mean planetary albedo partitioned between atmospheric and surface components.

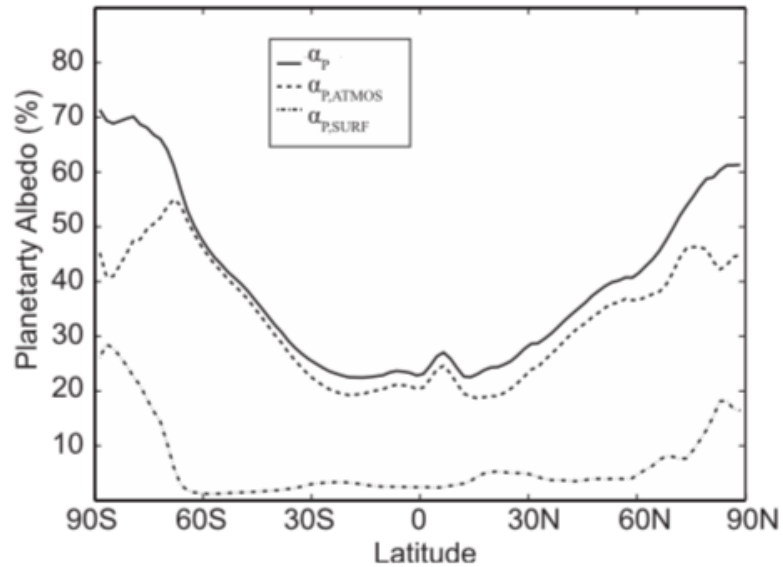


Figure 3: Zonal mean planetary albedo partitioned between atmospheric and surface components ¹⁰

In our model, we first approximate the total planetary albedo by choosing a reference planetary albedo α_{p0} of the form

$$\alpha_{p0} = \alpha_{p0}^0 + \alpha_{p0}^1 x^4, \quad (8)$$

The coefficients α_{p0}^0 and α_{p0}^1 are chosen along with parameters for the ground albedo in Eq (11) so that the equilibrium average planetary albedo given in Section 3 approximates Earth’s average planetary albedo, and in order to specify initial equilibrium locations of maximal absolute values of temperature gradients. Figure 4 shows a plot of α_{p0} for this choice of parameters: $\alpha_{p0}^0 = 0.25$ and $\alpha_{p0}^1 = 0.38$.

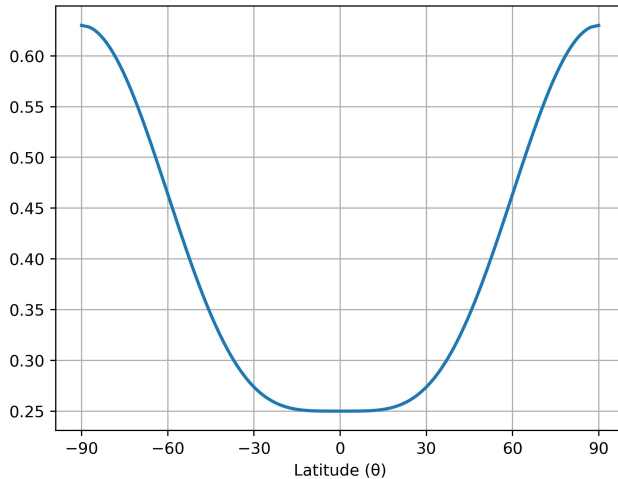


Figure 4: Initial planetary albedo with parameters chosen so that $\alpha_{p0} = 0.25 + 0.38x^4$

We emphasize that at no time step in our computational scheme does the function in Eq. (8) represent the planetary albedo in our models, which instead will vary in time in a way that depends on the global temperature distribution. We use α_{p0} , along with the cloud factor function \mathcal{C}_f , to define the atmospheric contribution to the planetary albedo as:

$$\alpha_a = \mathcal{C}_f(\alpha_{p0} - \alpha_{clear}) + \alpha_{clear}, \quad (9)$$

where α_{clear} is the clear sky (cloud free) albedo of the atmosphere which we take as constant, $\alpha_{clear} = 0.149$ [43]. An initial sample plot of the atmospheric albedo is given in Figure 5. We note that plots of α_a depend on \mathcal{C}_f , and in the sequel \mathcal{C}_f will in turn depend on temperature gradients, as described below, so the atmospheric albedo will also depend on temperature gradients.

¹⁰Image taken from Donohoe and Battisti [10]

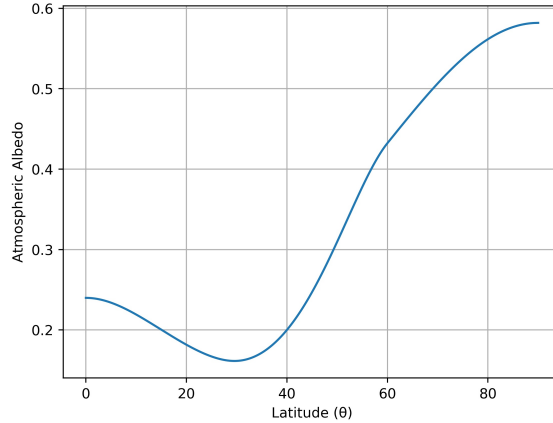


Figure 5: Initial atmospheric albedo α_a plotted as a function of latitude from equator to pole for cubic Hermite spline cloud factor $\mathcal{C}_f(\theta)$ using $\alpha_{p0_2} = 0.25 + 0.38x^4$ and the graph in Figure 2.

We can now define the atmospheric transmittance of short wave radiation (SWR) in terms of α_a as

$$\mathcal{T}_{sw} = 1 - \alpha_a - A_{sw}, \quad (10)$$

where $A_{sw} = 0.05$ is the atmospheric absorption of SWR [20]. We note that \mathcal{T}_{sw} depends on \mathcal{C}_f , making it interactive.

Following other researchers (for example [21]), we model the ground albedo as a function of the surface temperature using the hyperbolic tangent function as follows,

$$\alpha_g = 0.40 - 0.34 \tanh(T_s + 6.7). \quad (11)$$

2.3 Albedo Constraint

The fraction of incoming solar energy sent back to space from Earth is about 29% [43] with roughly 88% of that coming from the atmospheric contribution and the remainder due to the modulated surface albedo [10, 37]. We therefore restrict our atmospheric and modulated ground albedos to these approximate values. They are of necessity approximate because the atmospheric and ground albedo contributions in our model are dynamic and therefore fluctuate.

The total planetary albedo α_p is given by,

$$\alpha_p = \frac{1}{2} \int_{-1}^1 \alpha_p(x) s(x) dx \quad (12)$$

where, as before, x is the sine of latitude, $\alpha_p(x)$ is the zonally averaged albedo at x given by Eq. (6), and $s(x)$ is the annual weight function for incoming solar radiation given by equation 5. The planetary atmospheric albedo α_a is defined as,

$$\alpha_a = \frac{1}{2} \int_{-1}^1 \alpha_a(x) s(x) dx, \quad (13)$$

where $\alpha_a(x)$ is the zonally averaged atmospheric albedo at x . Therefore, we define the total planetary effective ground albedo by,

$$\overline{\mathcal{T}_e \alpha_g} = \alpha_p - \alpha_a \quad (14)$$

2.4 The Model

The energy balance equations in this section will be incorporated into what we describe as Model One and Model Two in Section 3, but with different dynamics of the cloud factor function. The algorithms for the dynamics are given in Subsection 2.5, and they depend on the equations for the climate model developed in this section.

We begin by linearizing the terms F_{up}, F_{out} in Eqs (1a) and (1b) and write,

$$\begin{aligned} F_{out} &= A_{out} + B_{out} T_a \\ F_{up} &= A_{up} + B_{up} (T_s - T_a), \end{aligned} \quad (15)$$

Then, collecting the remaining terms from the preceding sections, the system of coupled PDEs for the zonally and column averaged two layer climate system becomes,

$$\begin{aligned} C_a \frac{\partial T_a}{\partial t} &= (1 - \alpha_a - \mathcal{T}_{sw}) \left(1 + \frac{\alpha_g \mathcal{T}_{sw}}{1 - \alpha_a \alpha_g} \right) \frac{S_0 s(x)}{4} + A_{up} + B_{up} (T_s - T_a) \\ &\quad - A_{out} - B_{out} T_a + \frac{C_a K_a}{a^2} \frac{\partial}{\partial x} \left[(1 - x^2) \frac{\partial T_a}{\partial x} \right] \end{aligned} \quad (16a)$$

$$\begin{aligned} C_s \frac{\partial T_s}{\partial t} &= \frac{(1 - \alpha_g) \mathcal{T}_{sw}}{1 - \alpha_a \alpha_g} \frac{S_0 s(x)}{4} - A_{up} - B_{up} (T_s - T_a) \\ &\quad + \frac{C_s K_s}{a^2} \frac{\partial}{\partial x} \left[(1 - x^2) \frac{\partial T_s}{\partial x} \right] \end{aligned} \quad (16b)$$

$$\sqrt{1 - x^2} \frac{\partial T_a}{\partial x} \Big|_{x=-1,0,1} = \sqrt{1 - x^2} \frac{\partial T_s}{\partial x} \Big|_{x=-1,0,1} = 0; t > 0 \quad (16c)$$

Table 1 lists the parameter values appearing in Eqs. (16a) and (16b). These are the same choices made by Rose and Marshall [38, 39].

Parameter	Units	Numerical Value
a	m	6.373×10^6
S_0	$W m^{-2}$	1367
s_2		-0.48
C_a	$J m^{-2} \circ C^{-1}$	10^7
C_s	$J m^{-2} \circ C^{-1}$	10^7
K_a	$m^2 s^{-1}$	2.7×10^6
K_s	$m^2 s^{-1}$	5.2×10^5
B_{up}	$W m^{-2} \circ C^{-1}$	15
A_{up}	$W m^{-2}$	238
B_{out}	$W m^{-2} \circ C^{-1}$	1.7
A_{out}	$W m^{-2}$	211

Table 1: Parameter values for the EBM as in Rose and Marshall [38, 39].

The initial ($t = 0$) temperature profile is specified below, and the dynamic feature of the cloud factor function is explained in the following subsection.

The system of equations given in Sect.2.4 is defined for $-1 \leq x \leq 1$, where $x < 0$ is the Southern Hemisphere and $x > 0$ is the Northern Hemisphere. The Southern and Northern hemispheres are symmetric with respect to the boundary value problem. So, by symmetry, we need only consider the solution from $0 \leq x \leq 1$.

2.5 Cloud Function Dynamics and Polar Jet Stream

The response of eddy-driven jets and storm track latitudes to arctic amplification and changing meridional temperature gradients has been analyzed extensively (e.g., [4, 3, 13, 28, 30, 40, 50] and references therein). With the thermal wind equations in mind, we identify the mean latitudinal position of the polar jet stream, at any time t , with the location of the maximum value of a meridional temperature gradient in two different ways, which we refer to as Model One and Model Two.

1. Model One - We identify the location of the polar jet at any time t as the maximum absolute value of

$$\frac{\partial T_a(t, x)}{\partial x}. \quad (17)$$

This derivative is proportional to the rate of change of mid atmospheric temperature, T_a , with respect to the Euclidean distance, from the latitude with coordinate x , to the plane of the equator.

2. Model Two - In this case we identify the jet location with the maximum of the absolute value of the gradient of the average of the surface and atmospheric temperatures, i.e., as the absolute value of

$$\frac{1}{2} \frac{\partial}{\partial \theta} (T_a(t, \theta) + T_s(t, \theta)). \quad (18)$$

Other choices for temperature gradient, involving the atmospheric temperature, T_a , are possible. But unlike those of Models One and Two, the alternatives have been investigated and found to lead to less physical behavior of the cloud factor function in our model.

For each of the two models, the temperature gradients (17) and (18) are coupled in turn with the cloud factor function in the following way: We solve the model equations in Sect.2.4 numerically by time-stepping out to equilibrium (or quasi-periodicity). At each time step $t^n = n\Delta t$ of the numerical calculation, the cloud factor function \mathcal{C}_f is updated so that it takes the value 0.9 for all x greater than or equal to the value of x which maximizes the absolute value of the meridional temperature gradient, in the previous time step, for the model in question. For example, the graph in Figure 2 corresponds to a maximum meridional temperature gradient occurring at 60° latitude. Since the atmospheric albedo α_a depends on \mathcal{C}_f (c.f. Eq.(9)), it is updated in this way. Similarly, the ground albedo α_g (which is a function of latitude) is updated at each time step according to the value of the surface temperature T_s in the previous time step (see Eq.(11)). Numerical approximation details are described in Appendix B.

3 Numerical Results

In this section we present numerical results for our Model One and Model Two in response to increases in radiative forcing, such as from increased greenhouse gas concentrations. Following [38], to simulate increased greenhouse gas concentrations, we decrease the parameter A_{out} which controls the flux of outgoing longwave radiation (OLR) from the top of the atmosphere. Our focus is on how the latitudinal locations of the maximum modulus of temperature gradients, in equilibrium, given by Eqs. (17) and (18), are affected by these increases in radiative forcing. We interpret those latitudes as the averaged locations of the polar jet stream.

Since the coupled partial differential equations of the models are non autonomous, equilibrium temperature and temperature gradient values for each experiment must be found by numerically running them out to equilibrium¹¹. The results of this section take as initial temperature distributions the final equilibrium temperatures obtained by Rose and Marshall [38] (in their Figure 2), but the model behaviors are insensitive to the choice of initial temperature distributions.

3.1 Model One

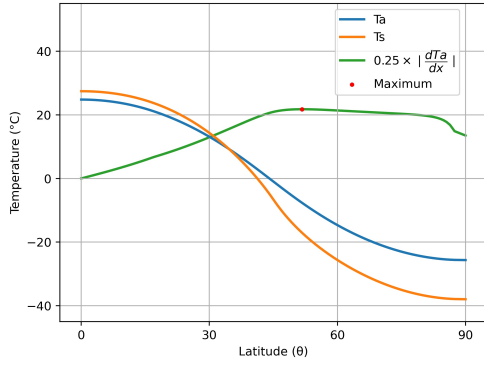
To set a reference climate for Model One, we take $A_{out} = 213.9 \text{ Wm}^{-2}$. In equilibrium, this yields a climate with a high planetary albedo, $\alpha_p = 0.337$, and cold average temperatures given by $T_s = 5.9^\circ\text{C}$ and $T_a = 8.0^\circ\text{C}$. The maximum absolute value of the atmospheric temperature gradient occurs at 51.7° latitude. This is our proxy for the average latitude of the jet stream. The temperature and gradient distributions are displayed in Figure 6(a).

By decreasing the parameter A_{out} , we introduce a radiative forcing to simulate an increase in greenhouse gas concentrations in the model. With a decrease to 213.5 Wm^{-2} of A_{out} , the average jet location begins to move poleward and at equilibrium reaches 58° latitude with global average temperatures of $T_s = 9.4^\circ\text{C}$ and $T_a = 11.1^\circ\text{C}$ and planetary albedo of .327. The temperature and gradient distributions are presented in Figure 6(b).

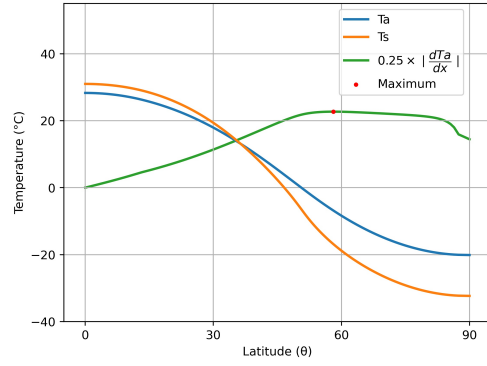
With $A_{out} = 213 \text{ Wm}^{-2}$ the global average temperatures and planetary albedo more closely resemble those of present day Earth, with $T_s = 14.4^\circ\text{C}$, $T_a = 15.6^\circ\text{C}$ and a planetary albedo of .300. The boundary of the polar cell increases to 62.1° latitude as displayed in Figure 6(c). As A_{out} decreases to 206 Wm^{-2} , the global average surface and atmospheric temperatures increase as does the boundary of the polar cell which reaches a maximum latitude of 80.0° , depicted in Figure 6(d).

However, as A_{out} decreases further, to values less than 206 Wm^{-2} , the movement of the polar jet location is reversed. It begins to decrease. When $A_{out} = 205 \text{ Wm}^{-2}$, the equilibrium location of the jet decreases to 78.5° latitude, as shown in Figure Figure 6(e). For $A_{out} = 203 \text{ Wm}^{-2}$, the jet location moves further equatorward to 77.7° latitude. See Figure 6(f).

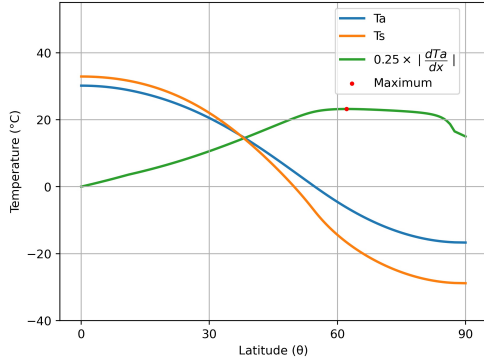
¹¹For low values of A_{out} , Model Two does not reach equilibrium with a constant location of the temperature gradient. Instead the maximum temperature gradient becomes quasi-periodic, oscillating between different latitudes, as elaborated below



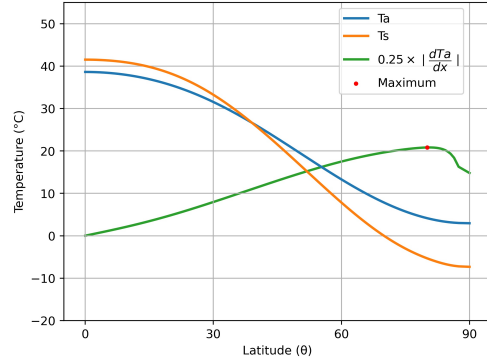
(a) $A_{out} = 213.9 W m^{-2}$



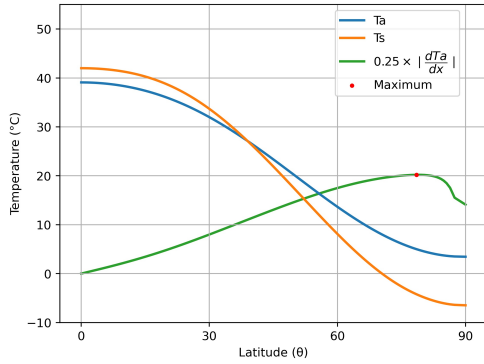
(b) $A_{out} = 213.5 W m^{-2}$



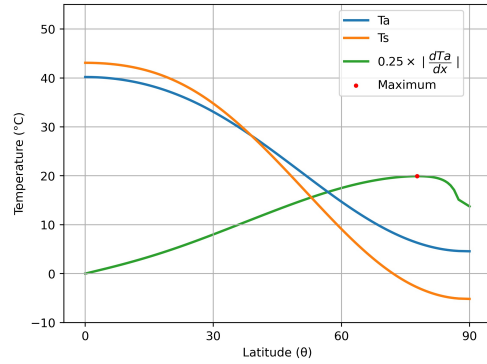
(c) $A_{out} = 213 W m^{-2}$



(d) $A_{out} = 206 W m^{-2}$



(e) $A_{out} = 205 W m^{-2}$



(f) $A_{out} = 203 W m^{-2}$

Figure 6: Model One meridional profiles of T_s and T_a with temperature gradients. Increased greenhouse gas concentrations are modeled by decreasing values of A_{out} . The maximum value of $|\partial T_a / \partial x|$ (scaled by a factor of 0.25 for display purposes) is indicated by a red dot which represents the average latitude of the polar jet under the indicated forcing of A_{out} . In plots (a) through (d), the jet moves poleward monotonically as A_{out} decreases, but in plots (e) and (f) the movement of the jet is reversed, moving equatorward as A_{out} decreases.

3.2 Model Two

Model Two exhibits a behavior not shared with Model One. With sufficient forcing (i.e., low values of A_{out}), the modulus of the temperature gradient given by Eq.(18) does not peak at a singular latitude, but instead produces a collection of nearly equal large values within an interval of latitudinal coordinates. As a physical interpretation, this suggests the emergence of instability of the jet stream.

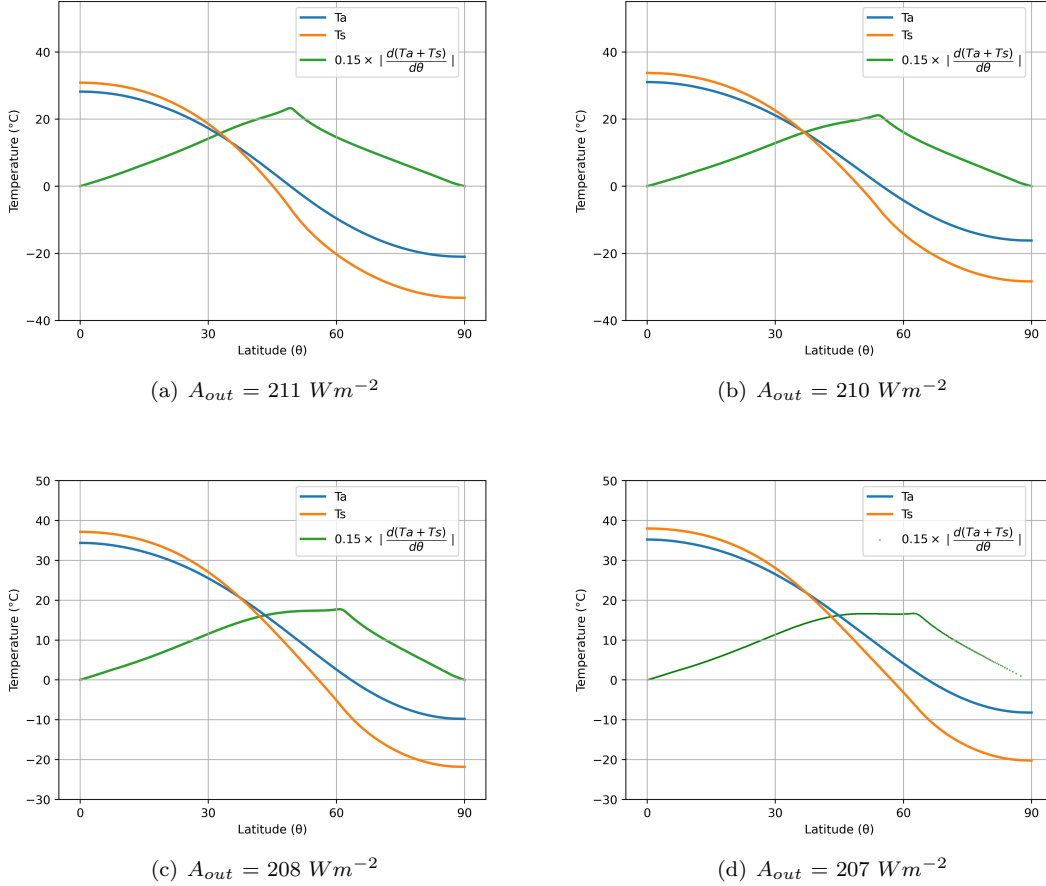


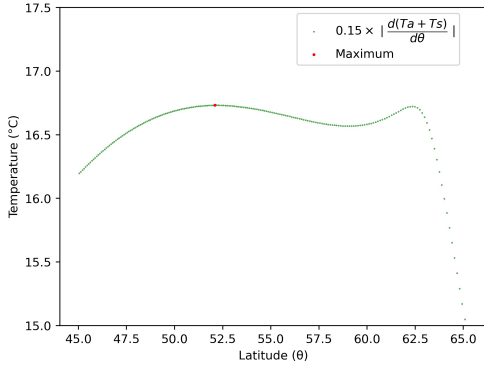
Figure 7: Model Two meridional profiles of T_s and T_a with and temperature gradients. Increased greenhouse gas concentrations are modeled by decreasing values of A_{out} . The maximum value of $|\partial/\partial\theta(T_a + T_s)|$ (scaled by a factor of 0.15 for display purposes) represents the average latitude of the polar jet under the indicated forcings of A_{out} . In plots (a) through (c), the jet moves poleward monotonically as A_{out} decreases, but plot (d) begins to form an approximate plateau with no fixed maximum location in equilibrium.

To explain this phenomenon, we start with $A_{out} = 211 \text{ Wm}^{-2}$, and then decrease it by integer values. The choice of $A_{out} = 211 \text{ Wm}^{-2}$ results in an equilibrium climate with planetary albedo, $\alpha_p = 0.324$, and global average temperatures given by $T_s = 14.9^{\circ}\text{C}$ and $T_a = 12.2^{\circ}\text{C}$. The maximum absolute value of the atmospheric temperature gradient occurs at 49.1° latitude, the proxy for the average latitude of the jet stream in this model. The temperature and gradient distributions are displayed in Figure 7(a). Thereafter, the location of the

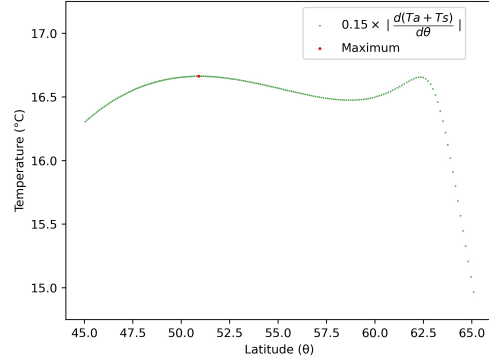
maximum modulus of the temperature gradient increases monotonically as A_{out} decreases until $A_{out} = 208 \text{ Wm}^{-2}$ for which the average jet stream location is 60.6° latitude, shown in Figure 7(c). At $A_{out} = 207$, Figure 7(d) shows the beginning of the formation of an approximate plateau of maximum values of the modulus of the temperature gradient.

Table 2: Average Locations of Max Temperature Gradients, Model Two

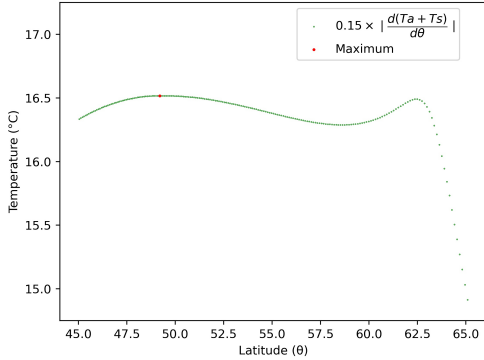
A_{out}	Mean Location of Unstable Jet	Standard Deviation
207 Wm^{-2}	61.0° latitude	3.22
206 Wm^{-2}	57.7° latitude	5.55
205 Wm^{-2}	55.0° latitude	6.60
204 Wm^{-2}	51.8° latitude	6.83



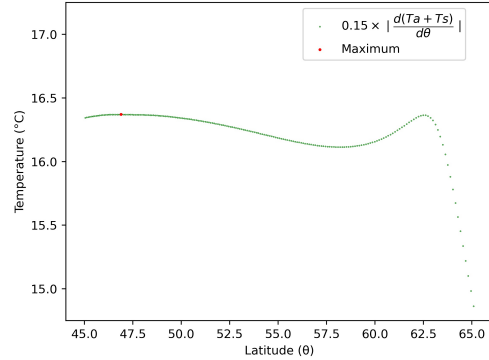
(a) $A_{out} = 207 \text{ Wm}^{-2}$



(b) $A_{out} = 206 \text{ Wm}^{-2}$



(c) $A_{out} = 205 \text{ Wm}^{-2}$



(d) $A_{out} = 204 \text{ Wm}^{-2}$

Figure 8: Sample maxima of $|\partial(T_a + T_s)/\partial\theta|$ indicated with a red dot, along with displays of approximate plateaus of maximum values, at particular time steps for unstable values of $A_{out} < 208$. With each time step the maximum on each plot shifts to a different latitude, see Appendix C.

Numerical calculations, displayed in Appendix C, show that the latitudinal locations of the maximum modulus of the temperature gradient are eventually

quasi-periodic, oscillating among a finite but increasing number of locations as A_{out} is decreased. The means and standard deviations of the latitudes of maximal moduli of the temperature gradients are displayed in Table 2. Figures 8(a) through 8(d) show portions of the weighted temperature gradient plots close to the maximum values.

4 Discussion

Our results may be compared with observations and predictions from more elaborate models. Using the Coupled Model Intercomparison Project (CMIP5) and assuming the representative concentration pathway 8.5 (RCP8.5) scenario, Barnes and Polvani [4] found that all jets migrate poleward in the twenty-first century. Using reanalysis, Manney and Hegglin [28] found that the southern polar jet has shown a robust poleward shift, while the northern polar jet has shifted equatorward in most regions and seasons. Liu et al. showed in [25] that in a simulation of the Last Glacial Maximum, NCAR’s CCSM4 model indicates that in the Southern Hemisphere the ice line advances equatorward while the jet shifts poleward. In [13] Francis and Vavrus found evidence to support a linkage between rapid Arctic warming and more frequent high-amplitude, wavy jet-stream configurations, and in [22] Karamperidou, Cioffi, and Lall considered meridional surface temperature gradients and found them to be determinants of large-scale atmospheric circulation patterns.

The behavior of our models share qualitative features with these investigations. A simulation of increased greenhouse gas concentrations results in an initial poleward movement of the polar jet, followed by an equatorward shift under greater forcings. In Model Two, the location of jet, under high concentrations, exhibits quasi-periodic behavior and instability. Our results may also be compared to those of MS18 [30] and SAR18 [40], both of which used EBMs to demonstrate the influence of changing Hadley cell boundaries on the location of mid-latitude storm tracks. Our results do not contradict those findings, but suggest that the latitudinal distribution of clouds may play a significant role as well.

References

- [1] Admin. (2019, March 6). Developer Reference for Intel®Math Kernel Library -C. Retrieved from <https://software.intel.com/en-us/mkl-developer-reference-c-gesv>
- [2] Angermann, L., & Knabner, P. (2003). *Numerical Methods for Elliptic and Parabolic Partial Differential Equations*. New York, NY: Springer.
- [3] Armour K.C., Siler, N., Donohoe, A., Roe, G. (2019). Meridional Atmospheric Heat Transport Constrained by Energetics and Mediated by Large-Scale Diffusion. *Journal of Climate*, 32, 3655-3690. doi:10.1175/JCLI-D-18-0563.1
- [4] Barnes, & E. A., Polvani, L. (2013). Response of the Midlatitude Jets, and of Their Variability, to Increased Greenhouse Gases in the CMIP5 Models. *Journal of Climate*, 26(18), 7117-7135. doi:10.1175/jcli-d-12-00536.1
- [5] Bonetti, F., McInnes, C. (2019) A continuous latitudinal energy balance model to explore non-uniform climate engineering strategies, *Climate Dynamics*, 52: 5739-5757. doi:10.1007/s00382-018-4474-y

- [6] Boucher, O., D. Randall, P. Artaxo, C. Bretherton, G. Feingold, P. Forster, V.-M. Kerminen, Y. Kondo, H. Liao, U. Lohmann, P. Rasch, S.K. Satheesh, S. Sherwood, B. Stevens and X.Y. Zhang, 2013: Clouds and Aerosols. In: Climate Change 2013: The Physical Science Basis. Contribution of Working Group I to the Fifth Assessment Report of the Intergovernmental Panel on Climate Change [Stocker, T.F., D. Qin, G.-K. Plattner, M. Tignor, S.K. Allen, J. Boschung, A. Nauels, Y. Xia, V. Bex and P.M. Midgley (eds.)]. Cambridge University Press, Cambridge, United Kingdom and New York, NY, USA.
- [7] Budyko, M. I. (1969). The Effect of Solar Radiation Variations on the Climate of the Earth. *Tellus*, 21(5), 611-619. doi:10.1111/j.2153-3490.1969.tb00466.x
- [8] Curry, J. A., Schramm, J. L., Rossow, W.B., & Randall, D. (1996). Overview of Arctic Cloud and Radiation Characteristics. *Journal of Climate*, 9(8), 1731-1764. doi:10.1175/1520-0442(1996)09<1731:OARCR>2.0.CO;2
- [9] Dima, I.M. and J.M. Wallace, 2003: On the Seasonality of the Hadley Cell. *Journal of the Atmospheric Sciences*, 60, 1522-1527, doi:10.1175/1520-0469(2003)060<1522:OTSOTH>2.0.CO;2
- [10] Donohoe, A., & Battisti, D. S. (2011). Atmospheric and Surface Contributions to Planetary Albedo. *Journal of Climate*, 24(16), 4402-4418. doi:10.1175/2011jcli3946.1
- [11] Dommenges, D., & Flöter, J. (2011) Conceptual understanding of climate change with a globally resolved energy balance model. *Clim Dyn*, 37 2143-2165, doi: 10.1007/s00382-011-1026-0
- [12] Emanuel, K. (2002) A Simple Model of Multiple Climate Regimes. *Journal of Geophysical Research: Atmospheres*, 107(D9), doi:10.1029/2001jd001002
- [13] Francis, J. A., & Vavrus, S. J., (2015). Evidence for a wavier jet stream in response to rapid Arctic warming. *Environmental Research Letters*, 10(1), 014005. doi:10.1088/1748-9326/10/1/014005
- [14] Golub, G. H., & Van Loan, C. F. (2007). Matrix Computations. Baltimore: Johns Hopkins Univ. Press.
- [15] Graversen, R. G., & Wang, M. (2009). Polar amplification in a coupled climate model with locked albedo. *Climate Dynamics*, 33(5), 629-643. doi: 10.1007/s00382-009-0535-6.
- [16] Held, I. M., & Suarez, M. J. (1974). Simple albedo feedback models of the icecaps. *Tellus*, 26(6), 613-629. doi:10.3402/tellusa.v26i6.9870
- [17] Hu, Y., Fu, Q. (2007) Observed poleward expansion of the Hadley circulation since 1979, *Atmos. Chem. Phys.*, 7, 5229-5236
- [18] Ikeda, T., & Tajika, E. (1999). A study of the energy balance climate model with CO₂ outgoing radiation: implication for the glaciation during the Cenozoic. *Geophysical Research Letters*, 26(3), 349-352.
- [19] IPCC, 2007: Climate Change 2007: The Physical Science Basis. Contribution of Working Group I to the Fourth Assessment Report of the Intergovernmental Panel on Climate Change [Solomon, S., D. Qin, M. Manning, Z. Chen, M. Marquis, K.B. Averyt, M. Tignor and H.L. Miller (eds.)]. Cambridge University Press, Cambridge, United Kingdom and New York, NY, USA, 996 pp.

- [20] Jentsch, V. (1991). An Energy Balance Climate Model with Hydrological Cycle: 1. Model Description and Sensitivity to Internal Parameters. *Journal of Geophysical Research*, 96(D9), 17169. doi:10.1029/91jd01478
- [21] Kaper, H. G., & Engler, H. (2013). *Mathematics and Climate*. Philadelphia, PA: SIAM.
- [22] Karamperidou, C., Cioffi, F., & Lall, U. (2012). Surface Temperature Gradients as Diagnostic Indicators of Midlatitude Circulation Dynamics. *Journal of Climate*, 25(12), 4154-4171. doi:10.1175/jcli-d-11-00067.1
- [23] Kiehl, J. T., & Trenberth, K. E. (1997). Earth's Annual Global Mean Energy Budget. *Bulletin of the American Meteorological Society*, 78(2), 197-208. doi: 10.1175/1520-0477(1997)078<0197:eagmebj2.0.co;2
- [24] Lindzen, R. S., & Farrell, B. (1977). Some Realistic Modifications of Simple Climate Models. *Journal of the Atmospheric Sciences*, 34, 1487-1501.
- [25] Liu, W., Lu, J., Leung, L.R., Xie, S-P, Liu, Z., Zhu J. (2015) The de-correlation of westerly winds and westerly-wind stress over the Southern Ocean during the Last Glacial Maximum, *Climate Dynamics*, 45:3157-3168, doi: 10.1007/s00382-015-2530-4
- [26] Liu, X., D.S. Battisti, and G.H. Roe, (2017), The Effect of Cloud Cover on the Meridional Heat Transport: Lessons from Variable Rotation Experiments. *Journal of Climate*, 30, 7465-7479, doi: 10.1175/JCLI-D-16-0745.1
- [27] Lu, J. Vecchi, G., Reichler, T. (2007) Expansion of the Hadley cell under global warming *Geophysical Research Letters*, 34 L18804 doi: 10.1029/2006GL028443
- [28] Manney, G. L., Hegglin, M. I. (2018). Seasonal and Regional Variations of Long-Term Changes in Upper-Tropospheric Jets from Reanalyses, *Journal of Climate*, 31(1), 423-448, doi: 10.1175/jcli-d-17-0303.1
- [29] Mbengue C. (2015). Storm Track Response to Perturbations in Climate. Dissertation (Ph.D.) California Institute of Technology. doi:10.7907/Z9FT8J05.
- [30] Mbengue C., Schneider, T. (2018). Linking Hadley Circulation and Storm Tracks in a Conceptual Model of the Atmospheric Energy Balance, *Journal of the Atmospheric Sciences*, 75, 841-856, doi: 10.1175/JAS-D-17-0098.1
- [31] Merlis, T.M. and Henry, M. (2018). Simple estimates of polar amplification in moist diffusive energy balance models. *Journal of Climate*, 31, 5811-5824, doi: 10.1175/JCLI-D-17-0578.1
- [32] North, G. R. (1975). Analytical Solution to a Simple Climate Model with Diffusive Heat Transport. *Journal of the Atmospheric Sciences*, 32(7), 1301-1307. doi:10.1175/1520-0469(1975)032<1301:astascj2.0.co;2
- [33] North, G. R., Cahalan, R. F., & Coakley, J. A. (1981). Energy Balance Climate Models. *Reviews of Geophysics*, 19(1), 91-121. doi:10.1029/rg019i001p00091
- [34] North, G. R., Mengel, J. G., & Short, D. A. (1983). Simple Energy Balance Model Resolving the Seasons and the Continents: Application to the Astronomical Theory of the Ice Ages. *Journal of Geophysical Research*, 88(C11), 6576. doi:10.1029/jc088ic11p06576

- [35] Palm, S. P., Strey, S. T., Spinhirne, J., & Markus, T. (2010). Influence of Arctic Sea Ice Extent on Polar Cloud Fraction and Vertical Structure and Implications for Regional Climate. *Journal of Geophysical Research*, 115(D21). doi:10.1029/2010jd013900.
- [36] Perillo, C. (2018). General Atmospheric Circulation in an Energy Balance Model. California State University, Northridge, Dept. of Mathematics.
- [37] Qu, X., & Hall, A. (2005). Surface Contribution to Planetary Albedo Variability in Cryosphere Regions. *Journal of Climate*, 18(24), 5239-5252. doi:10.1175/jcli3555.1.
- [38] Rose, B. E., & Marshall, J. (2009). Ocean Heat Transport, Sea Ice, and Multiple Climate States: Insights from Energy Balance Models. *Journal of the Atmospheric Sciences*, 66(9), 2828-2843. doi:10.1175/2009jas3039.1.
- [39] Rose, B. E. (2010). Oceanic Control of the Sea Ice Edge and Multiple Equilibria in the Climate System. Thesis (Ph.D.) Massachusetts Institute of Technology, Dept. of Earth, Atmospheric, and Planetary Sciences.
- [40] Siler, N., Roe, G.H., & Armour, K.C. (2018). Insights into the Zonal-Mean Response of the Hydrologic Cycle to Global Warming from a Diffusive Energy Balance Model. *Journal of Climate*, 31, 7481-7493. doi:/10.1175/JCLI-D-18-0081.1
- [41] Sellers, W. D. (1969). A Global Climatic Model Based on the Energy Balance of the Earth-Atmosphere System. *Journal of Applied Meteorology*, 8(3), 392-400. doi:10.1175/1520-0450(1969)0082.0.co;2.
- [42] Södergren, A. H., McDonald, A. J., & Bodeker, G. E. (2017). An energy balance model exploration of the impacts of interactions between surface albedo, cloud cover and water vapor on polar amplification. *Climate Dynamics*, 51(5-6), 1639-1658. doi:/10.1007/s00382-017-3974-5
- [43] Stephens, G. L., O'Brien, D., Webster, P. J., Pilewski, P., Kato, S., & Li, J. (2015). The Albedo of Earth. *Reviews of Geophysics*, 53(1), 141-163. doi:10.1002/2014rg000449.
- [44] Stocker, T. (2011). *Introduction to Climate Modeling*. Heidelberg: Springer.
- [45] Stocker, T. F., Mysak, L. A., & Wright, D. G. (1992). A Zonally Averaged, Coupled Ocean-Atmosphere Model for Paleoclimate Studies. *Journal of Climate*, 5(8), 773-797. doi:10.1175/1520-0442(1992)0052.0.co;2.
- [46] Stone, P. H., (1978). Constraints on dynamical transports of energy on a spherical planet. *Dyn. Atmos. Oceans*, 2, 123-139, doi:10.1016/0377-0265(78)90006-4
- [47] Strikwerda, J. C. (2004). *Finite Difference Schemes and Partial Differential Equations*. Philadelphia: SIAM.
- [48] The SciPy Community. (2019, January 31). Numpy.gradient. Retrieved from <https://docs.scipy.org/doc/numpy/reference/generated/numpy.gradient.html>
- [49] Vavrus, S., Waliser, D., Schweiger, A., & Francis, J. (2008). Simulations of 20th and 21st Century Arctic Cloud Amount in the Global Climate Models Assessed in the IPCC AR4." *Climate Dynamics*, 33(7-8), 1099-1115. doi:10.1007/s00382-008-0475-6.

- [50] Yin, J. H., (2005). A consistent poleward shift of the storm tracks in simulations of 21st century climate. *Geophys. Res. Lett.*, 32, L18701, doi:10.1029/2005GL023684
- [51] Zhou, C., Lu, J., Hu, Y., Zelinka, M.D. (2020). Responses of the Hadley Circulation to Regional Sea Surface Temperature Changes, *Journal of Climate*, 33, 2, (429-441), doi:10.1175/JCLI-D-19-0315.1

Appendices

A Cloud Factor Function Formulas

The formula for a cloud factor function is shown here. The Hadley cell boundary is taken as 30° latitude and the first extratropical maximum occurs at 60° latitude. The formula for the graph displayed in Figure 2 is given by

$$C_f(\theta) = \begin{cases} 0.0001111111(\frac{30-\theta}{15} + 1)\theta^2 + 0.001(\frac{\theta}{15} + 1)(30 - \theta)^2 & 0 \leq \theta \leq 30 \\ 0.0001111111(1 + \frac{\theta-30}{15})(60 - \theta)^2 + 0.001(1 + \frac{60-\theta}{15})(\theta - 30)^2 & 30 \leq \theta \leq 60 \\ 0.001(\frac{\theta-60}{15} + 1)(90 - \theta)^2 + 0.001(\frac{90-\theta}{15} + 1)(\theta - 60)^2 & 60 \leq \theta \leq 90 \end{cases} \quad (19)$$

B Solution Methodology For The Initial Boundary Value Problem

The initial boundary value problem (IBVP) (16) falls in the class of linear evolution problems for which various numerical methods have been developed. We have employed in this paper an *implicit* finite difference method (FDM) based on the Crank-Nicholson scheme [2, 47]. This scheme has the desirable property of being inherently *stable*. More specifically, we subdivide the spatial variable interval [0,1] uniformly in I subintervals (x_i, x_{i+1}) , $i = 0, \dots, I$ where $x_i = i\Delta x$; Δx being the spatial step size that is set to be 10^{-3} (See Figure 9). Similarly, we consider for the time variable t, the equidistant sequence $t^n = n\Delta t$; $n = 0, 1, \dots, N$, where the time step Δt is set to be 1 and N is chosen large enough for the temperature to reach the asymptotic regime, i.e, the equilibrium of the solution of the IBVP(16). For the simplicity of the publication, we introduce the auxiliary variable T to denote either the temperature of the atmospheric layer, T_a or the temperature of the surface layer, T_s . We then approximate $T(x_i, t^n)$ by T_i^n where T_i^n is the solution of the algebraic system resulting from the adopted finite difference scheme.

The derivatives that occur in the IBVP (16) are approximated as follows. First, we have distributed the spatial derivative and then we have used the following *second order* approximation,

$$\frac{\partial T}{\partial x}(x_i, t^n) \approx \frac{T_{i+1}^n - T_{i-1}^n}{2\Delta x} \quad (20)$$

and

$$\frac{\partial^2 T}{\partial x^2}(x_i, t^n) \approx \frac{T_{i+1}^n - 2T_i^n + T_{i-1}^n}{\Delta x^2} \quad (21)$$

The first order time derivative is replaced by a *second order* approximation using the Crank-Nicholson relations [2, 47]

$$\frac{\partial T}{\partial t}(x_i, t^{n+\frac{1}{2}}) = \frac{1}{2} \left[\frac{\partial T}{\partial t}(x_i, t^{n+1}) + \frac{\partial T}{\partial t}(x_i, t^n) \right] \quad (22)$$

and

$$\frac{\partial T}{\partial t}(x_i, t^{n+\frac{1}{2}}) \approx \frac{T_i^{n+1} - T_i^n}{\Delta t} \quad (23)$$

sequentially, IBVP(16) is then replaced by the following algebraic system,

$$\begin{aligned} \beta(T_{a_i}^{n+1} - T_{a_i}^n) &= \frac{1}{2}[\beta'_i(T_{a_{i+1}}^{n+1} - 2T_{a_i}^{n+1} + T_{a_{i-1}}^{n+1}) - \beta''_i(T_{a_{i+1}}^{n+1} - T_{a_{i-1}}^{n+1}) \\ &\quad - (B_{up} + B_{out})T_{a_i}^{n+1} + B_{up}T_{s_i}^{n+1} + A_{up} - A_{out} \\ &\quad + (1 - \alpha_{a_i}^n - \mathcal{T}_{sw_i}^n)(1 + \frac{\alpha_{g_i}^n \mathcal{T}_{sw_i}^n}{(1 - \alpha_{a_i}^n \alpha_{g_i}^n)}) \frac{S_0 s(x_i)}{4} \\ &\quad + \beta'_i(T_{a_{i+1}}^n - 2T_{a_i}^n + T_{a_{i-1}}^n) - \beta''_i(T_{a_{i+1}}^n - T_{a_{i-1}}^n) \\ &\quad - (B_{up} + B_{out})T_{a_i}^n + B_{up}T_{s_i}^n + A_{up} - A_{out} \\ &\quad + (1 - \alpha_{a_i}^n - \mathcal{T}_{sw_i}^n)(1 + \frac{\alpha_{g_i}^n \mathcal{T}_{sw_i}^n}{(1 - \alpha_{a_i}^n \alpha_{g_i}^n)}) \frac{S_0 s(x_i)}{4}] \end{aligned} \quad (24a)$$

$$\begin{aligned} \gamma(T_{s_i}^{n+1} - T_{s_i}^n) &= \frac{1}{2}[\gamma'_i(T_{s_{i+1}}^{n+1} - 2T_{s_i}^{n+1} + T_{s_{i-1}}^{n+1}) - \gamma''_i(T_{s_{i+1}}^{n+1} - T_{s_{i-1}}^{n+1}) \\ &\quad - B_{up}T_{s_i}^{n+1} + B_{up}T_{a_i}^{n+1} - A_{up} + \frac{(1 - \alpha_{g_i}^n) \mathcal{T}_{sw_i}^n}{(1 - \alpha_{a_i}^n \alpha_{g_i}^n)} \frac{S_0 s(x_i)}{4} \\ &\quad + \gamma'_i(T_{s_{i+1}}^n - 2T_{s_i}^n + T_{s_{i-1}}^n) - \gamma''_i(T_{s_{i+1}}^n - T_{s_{i-1}}^n) \\ &\quad - B_{up}T_{s_i}^n + B_{up}T_{a_i}^n - A_{up} + \frac{(1 - \alpha_{g_i}^n) \mathcal{T}_{sw_i}^n}{(1 - \alpha_{a_i}^n \alpha_{g_i}^n)} \frac{S_0 s(x_i)}{4}] \end{aligned} \quad (24b)$$

where

$$\begin{aligned} \beta &= \frac{C_a}{\Delta t} & \gamma &= \frac{C_s}{\Delta t} \\ \beta'_i &= \frac{C_a K_a (1 - x_i^2)}{2a^2 \Delta x^2} & \gamma'_i &= \frac{C_s K_s (1 - x_i^2)}{2a^2 \Delta x^2} \\ \beta''_i &= \frac{2x_i C_a K_a}{4a^2 \Delta x} & \gamma''_i &= \frac{2x_i C_s K_s}{4a^2 \Delta x} \end{aligned} \quad (25)$$

A schematic interpretation or cone of dependance of the adopted FDM discretization is depicted in Figure 9. It shows the implicit nature of this scheme. It also reveals that the evaluation of the temperature at the boundaries T_0^n (resp. T_I^n) requires the values of T_{-1}^n (resp. T_{I+1}^n). These ‘‘fictitious’’ values are set to be $T_{-1}^n = T_0^n$ and $T_{I+1}^n = T_I^n$; $n = 0, \dots, N$. This choice results from the *first order* approximation of the boundary condition, IBVP (16).

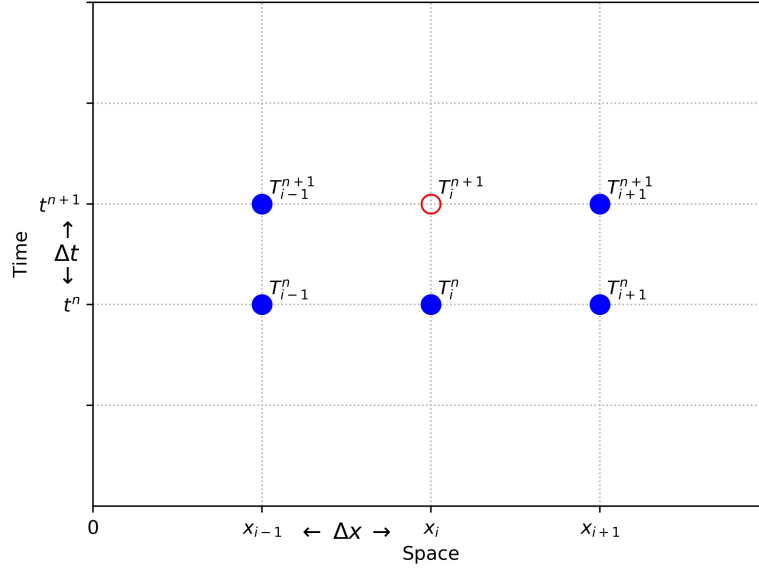


Figure 9: A schematic interpretation of the FDM approximation. The value of T_i^{n+1} (hollow disk) requires the values of five neighbored points (solid disks).

Note that the algebraic system (24) can be expressed in a compact representation as follows,

$$\mathbf{A}\mathbf{T}^{n+1} = \mathbf{B}\mathbf{T}^n + \mathbf{b}^n \quad (26)$$

Where A and B are block diagonal matrices whose entries are explicitly given in equations C.1 - C.14, pages 88 - 92 in [36]. The linear system (26) is solved using LPACK package (*routine -gesv*)[1] that is based on LU type decomposition [14].

The temperature gradients reported in Figures 6 - 8 have been evaluated with the software package (*numpy.gradient*)[48]. This routine computes the gradient using second order accurate central differences in the interior points and either first or second order accurate one-side differences at the boundaries.

C Quasi-Periodic Oscillations of Polar Jet in Model Two for Large Forcings

Table 3: Model Two Latitudes of Polar Jet defined by $\max |\partial/\partial\theta(T_a + T_s)|$ for $t^n \in [8725, 8760]$, the asymptotic regime of its solutions.

$A_{out} = 207$	$A_{out} = 206$	$A_{out} = 205$	$A_{out} = 204$
62.252	50.896	62.375	48.417
62.252	62.252	49.464	47.138
62.252	62.252	62.375	46.469
62.252	51.169	49.641	62.375
62.252	62.252	48.331	48.331
62.252	50.896	62.375	46.970
62.252	62.252	49.200	62.375
52.940	62.252	62.375	47.988
62.252	51.169	49.464	46.719
62.252	62.252	62.375	62.375
62.252	50.896	49.641	48.417
62.252	62.252	48.331	47.138
62.252	62.252	62.375	62.375
52.655	51.169	49.200	48.590
62.252	62.252	62.375	47.307
62.252	50.896	49.464	46.970
62.252	62.252	62.375	62.375
62.252	62.252	49.641	48.159
52.467	51.169	48.331	46.803
62.252	62.252	62.375	62.375
62.252	50.896	49.200	48.417
62.252	62.252	62.375	47.138
52.279	62.252	49.464	62.375
62.252	51.169	62.375	48.504
62.252	62.252	49.641	47.307
62.252	50.896	48.331	46.886
52.186	62.252	62.375	62.375
62.252	62.252	49.200	48.245
62.252	51.169	62.375	46.886
62.252	62.252	49.464	62.375
52.186	50.896	62.375	48.417
62.252	62.252	49.641	47.054
62.252	62.252	48.331	62.375
62.252	51.169	62.375	48.504
52.092	62.252	49.200	47.307
62.252	50.896	62.375	46.886